energies

MDPI

Article

Improving the Irradiance Data Measured by Silicon-Based Sensors

Riyad Mubarak *, Holger Schilke * and Gunther Seckmeyer *

Institute for Meteorology and Climatology, Leibniz Universität Hannover, Herrenhäuser Straße 2, 30419 Hannover, Germany

* Correspondence: mubarak@muk.uni-hannover.de (R.M.); schilke@muk.uni-hannover.de (H.S.); seckmeyer@muk.uni-hannover.de (G.S.)

Abstract: Silicon-based sensors are widely used for monitoring solar irradiance, in particular, in the field of Photovoltaic (PV) applications. We present a method to correct the global horizontal irradiance measured by silicon-based sensors that reduces the difference to the standard thermopile sensor measurements. A major motivation to use silicon-based sensors for the measurements of irradiance is their lower cost. In addition, their response time is much lower, and their spectral response is much closer to that of the PV systems. The analysis of the differences is based on evaluating four parameters that influence the sensor measurements, namely the temperature, cosine error, spectral mismatch, and calibration factor. Based on the analysis, a correction model is applied to the silicon sensors measurements. The model separates measurements under a clear sky and cloudy sky by combining the clearness index and the solar zenith angle. By applying the correction model on the measurements of the silicon-based sensor, the differences between sensor readings have been reduced significantly. The relative root mean squared difference (rRMSD) between the daily solar irradiation measured by both sensors decreased from 10.6% to 5.4% after applying the correction model, while relative mean absolute difference (rMAD) decreased from 7.4% to 2.5%. The difference in total annual irradiation decreased from 70 KWh/m^2 (6.5%) to 15 kWh/m^2 (1.5%) by the correction. The presented correction method shows promising results for a further improvement in the accuracy of silicon-based sensors.

Keywords: incident solar radiation; pyranometer; silicon sensors; solar reference cell

Citation: Mubarak, R.; Schilke, H.; Seckmeyer, G. Improving the Irradiance Data Measured by Silicon-Based Sensors. *Energies* **2021**, *14*, 2766. https://doi.org/10.3390/en14102766

Academic Editor: Jose A. Afonso

Received: 8 April 2021
Accepted: 8 May 2021
Published: 12 May 2021

1. Introduction

Solar irradiance provides the energy that powers the earth's climate and biosphere. This energy is the primary source for many processes on earth, including processes that sustain living systems and circulation of the atmosphere and oceans [1]. This energy is also readily available for providing electricity and heat for industrial and domestic applications [2]. Accurate measurements of solar irradiance are needed for understanding the primary source of energy input to the earth–atmosphere–ocean system and for evaluation of photovoltaic (PV) power profiles [3]. Moreover, solar irradiance is the most important input parameter for PV software to predict the expected solar energy.

The global horizontal irradiance (GHI) is the most commonly measured component of solar radiation [4] and includes both direct beam and diffuse radiation. GHI is of particular interest to photovoltaic installations and is defined as the total solar radiation per unit area that is intercepted by a flat, horizontal surface.

Due to the increasing interest in solar energy and climate changes, solar irradiance measurements are gaining higher importance compared to recent years. According to IPCC [5], a small variation in solar irradiance can produce natural forcing of earth's climate with global and regional-scale responses. Therefore, accurate irradiance measurements are essential for the detection and attribution of climate change [6].

Instruments measuring solar irradiance may be classified as thermal sensors (thermopile pyranometers) and silicon-based (PV) sensors. Radiometers equipped with thermal sensors are widely used to measure broadband solar irradiance due to their nearly constant spectral response over the whole solar spectral range [7]. However, thermal sensors are costly in terms of hardware and calibration.

On the other hand, silicon-based radiation sensors provide the simplest and cheapest alternative. However, these sensors only respond to wavelengths between 300 and 1200 nm, and their spectral response within this interval is not uniform. The response to the red and near-infrared light is noticeably higher than for blue and ultraviolet light. This limited and non-uniform spectral response causes a spectral mismatch of the broadband irradiance measurement [8].

Many studies have highlighted the differences between both sensors and evaluated the uncertainties for solar radiation measurements. Understanding these differences is important because PV system performance analysis often depends on accurate solar irradiance data, and sensors of different technologies may be used. Dunn et al. [9] calculated typical measurement uncertainties for PV sensor and thermopile pyranometer measurements. The calculations were performed for a fixed-tilt system under clear sky conditions. They found the uncertainties in irradiance measurements to be in the order of $\pm$2.4% for PV reference devices and $\pm$5% for thermopile pyranometers. Meydbray et al. [10] considered the spectral effect and calculated the deviation of the two sensors in four different locations in the USA. They found that the daily solar irradiation deviation can amount up to 3% and that this deviation is highly variable over days, weeks, and months. Azouzoute et al. [11] compared the Plane of Array irradiance data, measured at a tilt plan of 32° by a first-class thermopile sensor and a reference PV cell. They found that the monthly deviation between the solar irradiation measurements from both devices ranges between $-$4.8% in June to $-$0.7% in December. Several researchers have developed correction methods that reduce the systematic errors of silicon sensors. The temperature correction is almost similar in all versions, while the methods used to correct the spectral effects vary between the publications. The corrections depend on the sensor temperature, the solar zenith angle (SZA), air mass (AM), diffuse horizontal irradiance (DHI), and global horizontal irradiance (GHI).

In the following, we present different approaches for spectral corrections. Alados-Arboledas et al. [12] used tabular factors for different sky parameters and a functional correction depending on the solar incidence angle. King and Myers [13] proposed functional corrections based on air mass and the angle of incidence derived for global irradiation. Vignola [14] further developed this approach and included diffuse and subsequently direct beam irradiance. Moreover, the German Aerospace Center (DLR) has developed a method using functional corrections, including a particular spectral parameter. The method was developed in 2003 and based on global, diffuse, and direct irradiance [15]. Forstinger et al. [16] suggested a new correction and calibration method based on a physical approach. The method aimed to remove the systematic errors and is based on information of the sensor properties, which includes its directional response and the site's atmospheric conditions.

This study aims to examine the differences in the readings of thermopile pyranometer and silicon sensor at a timescale of minutes, days, months, and years in Hannover. The goal is to evaluate the irradiance data from each sensor, identify contributing factors behind the variations between the readings, and create simple empirical correction methods that require a minimum number of inputs to improve the silicon sensor measurements and reduce the differences between both sensors.

2. Instruments

The measurement system installed on the rooftop of IMUK consists of different meteorological and radiation instruments. The systems have been described shortly in Mubarak et al. [17,18]. We will focus only on the irradiance devices, as their data will be used in this work, namely the thermopile pyranometers and silicon-based sensors.

2.1. Thermopile Pyranometer

Pyranometers are broadband instruments that measure global solar irradiance received from the whole skydome (2 Ω solid angle). Besides global irradiance, pyranometers can also measure diffuse irradiance. For this, a small shading disk can be mounted on an automated solar tracker. Alternatively, a shadow ring may prevent the direct component from reaching the sensor the whole day. The International Standard [19] and the World Meteorological Organization (WMO) distinguishes three classes of pyranometers based on performance characteristics and specifications: the best class is called secondary standard, the second-best is called first class, and the third is called second-class. The thermopile sensors used in this study are CMP11 pyranometers from Kipp & Zonen [20] (hereafter referred to simply as Pyr). The sensors were used to measure GHI and DHI.

A typical pyranometer (Figure 1) consists of a black-painted disk (detector) sealed by two glass domes, which protect the sensor from thermal convection and weather threat (e.g., rain and wind). The double glass domes also limit the instrument's spectral sensitivity in the wavelength range between 280 nm and 2800 nm and usually have a bubble for silicon-based. Moreover, the specially designed double glass domes also produce a more accurate angular response in the instrument and reduce thermal losses [21].

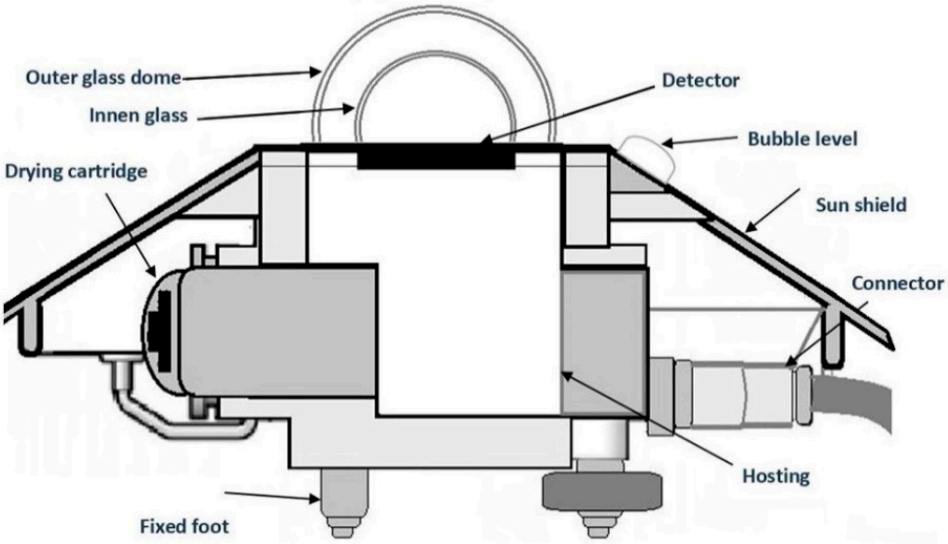

Figure 1. Thermopile Pyranometer.

2.2. Silicon Sensors

During the last decade, silicon-based sensors have been used as low-cost radiation instruments to monitor PV plants [22]. Silicon-based sensors have a similar spectral response (300–1200 nm) as a solar panel. As a result, silicon sensors provide a more accurate representation of the energy available for conversion to electricity by a solar panel at a tenth of the cost of a thermopile pyranometer [23]. In general, there exist two main types of silicon sensors to monitor PV solar systems, specifically silicon-photodiode pyranometers and reference solar cells. A photodiode-based pyranometer essentially monitors the short circuit current of a solar cell under a diffusing lens. The pyranometer body and diffusing lens are designed to minimize deviations from a true angular response [22]. However, the irradiance values indicated by these pyranometers, without correction, may differ from the "true" broadband solar irradiance by over 10% [24].

Unlike photodiode-based pyranometers, reference cells do not contain a diffuser; they have glazing, which allows as much of the incident solar radiation as possible to pass inside, such as PV modules (see Figure 2). Reference solar cells are expected to have a similar spectral response as photodiode-based pyranometers since photodiodes and reference cells are both solar cells for which the output is monitored in a short circuit configuration [21].

Generally, reference cells have an internal temperature measurement that can be used to adjust the temperature dependence of the measured irradiance.

Silicon sensors used in this research are monocrystalline solar cells from Ingenieurbüro Mencke and Tegtmeyer (IMT) [25] (hereafter referred to simply as SiS). The solar cells are in an aluminum casing with a glass cover and a Pt100 temperature sensor to measure the cell temperature. According to manufacturer specifications, the sensor's reading should agree within 5% with the thermopile pyranometer's reading within an ambient temperature between −20 to 70 °C and normal incident irradiance.

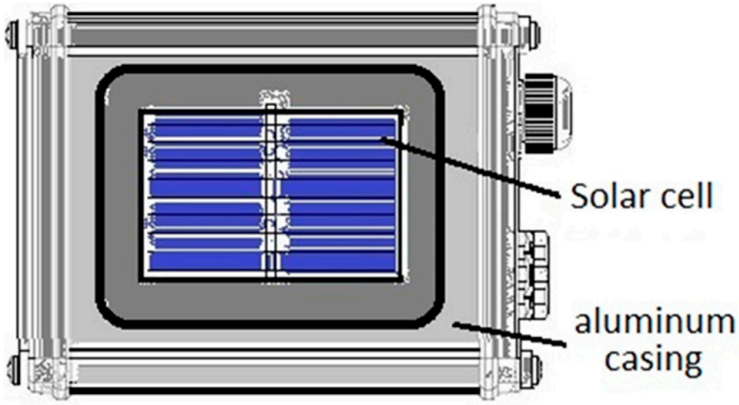

Figure 2. Silicon sensor (SiS) from IMT [26].

Measurements of both sensors were carried out from January 2016 to December 2019. The data were stored in data loggers. The loggers recorded all data, such as irradiation and temperature, from the sensors every one minute. In the following, the main differences between sensors will be discussed.

2.3. Differences between Sensors

As explained above, both sensors demonstrate differences in the used technology, measuring principle, and reactions to incident solar irradiance, as well as making differences in measured irradiance (Table 1). The main differences between the sensors will be further demonstrated and discussed.

Table 1. Analysis of the differences between sensors (linear calibration, offset, spectral response, angular response according to the manufacturers [20,25]).

Specifications	CMP11	Si-mV-85
Spectral sensitivity range (nm)	285–2800	360–1200
Response time (s)	<5	<0.001
Offset (W/m^2)	<2	0
Temperature dependence (−20–40 °C) (%)	<1	0.2
Uncertainty (W/m^2)	<5	±5
Non-linearity (100 to 1000 W/m^2) (%)	<0.2	±0.1
Angular response (% up to 80° SZA)	<1	<30

2.3.1. Temperature Response

The influence of temperature on the irradiance sensor signal is lower in thermopile pyranometers [26,27] than in silicon devices [13,28]. The different reaction of sensors to temperature is due to the different measurement principle. In the case of silicon-based sensors, the temperature affects the short circuit current of monocrystalline silicon cells; it records higher values at higher temperatures [29]. The used silicon sensors do not have a temperature compensation that reduces temperature dependence. Accordingly, the temperature change during the measurements should be taken into account and corrected. The

available SiS have internal temperature sensors that can be used to adjust the temperature dependence of the measured irradiance.

2.3.2. Spectral Response

The spectral response (SR) describes the sensor's sensitivity to radiation of different wavelengths. As defined, thermopile pyranometers measure solar irradiance within a wide wavelength range (290–2800 nm). Unlike thermopile pyranometers, silicon sensors do not respond to all incident wavelengths equally. Thus, they have a non-flat spectral response (Figure 3). The SR of silicon describes how well a material can utilize the light of a specific wavelength to generate an electric current. The SR of a silicon-based sensor has an upper limit of approximately 1200 nm, which is mainly determined by the spectral response of the used PV material. The spectral response of the used SiS has been shown in previous work [17].

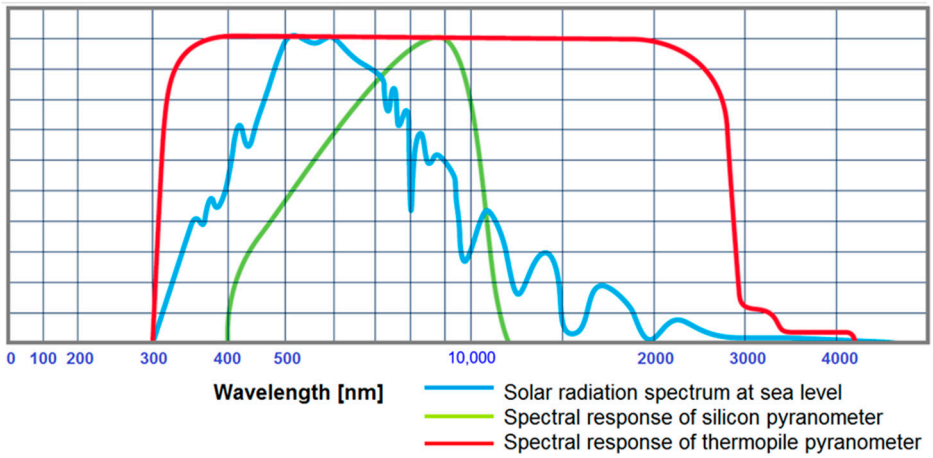

Figure 3. Spectral response curves of silicon, thermopile pyranometers, and solar spectrum at sea level [20].

2.3.3. Angular Response

The angular "cosine" response reflects the fact that the response of the irradiance sensor varies with the angle of incidence [30]. Global irradiance is measured with instruments assumed to have a true angular response. However, we know from different studies [31–33] that no instrument is perfect in this regard. The deviation of global irradiance measurements from the ideal cosine law is known as cosine error. The angular response of thermopile pyranometers is determined by the glass domes and the spectral and spatial uniformity of the thermopile detector. The used thermopile pyranometer has a good angular response, where the maximum deviation from the ideal angular response is less than 10 W/m^2 (up to an incidence angle of 80°) with respect to 1000 W/m^2 irradiance at normal incidence (0°) [34].

The angular response of a silicon sensor can be described as the reduction in sensor output when solar radiation impinges at angles deviating from the normal to the surface. This deviation affects the calibration of sensors and introduces energy losses in photovoltaic conversion. King et al. [13] attributed this decrease to two sources: The first one is a geometrical factor (cosine law). The second source results from the optical properties of the used sensor, primarily from the reflectance of input optics. The influence of incidence angle on the SiS response is shown in Figure 4. With an increasing incidence angle, the relative deviation rises significantly.

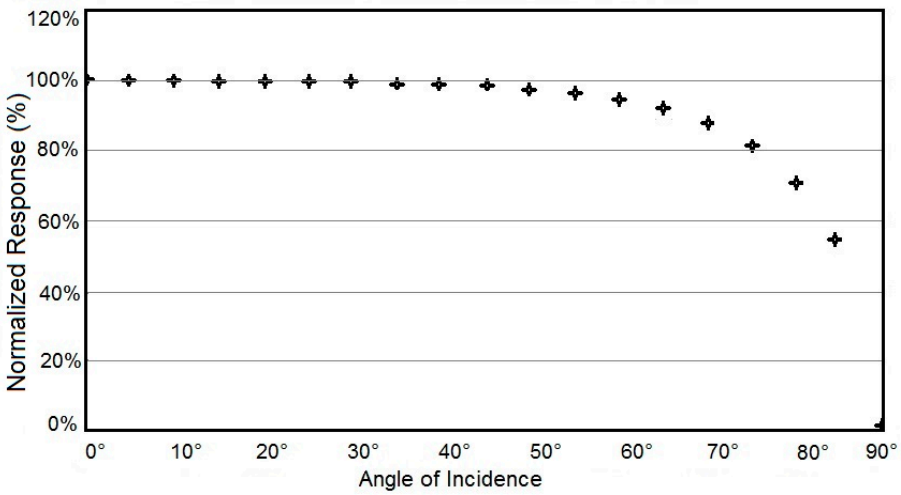

Figure 4. Normalized angular response of SiS versus solar angle-of-incidence measured by the manufacturer [25] under STC.

Figure 5 shows the difference between GHI measured by the Pyr and that measured by the SiS under a clear sky and overcast conditions. Under clear sky conditions, the Pyr measured higher irradiance, and the difference between both sensors increases in the morning and evening hours when the solar zenith angle is high. This may mainly be due to the higher cosine error of the used SiS.

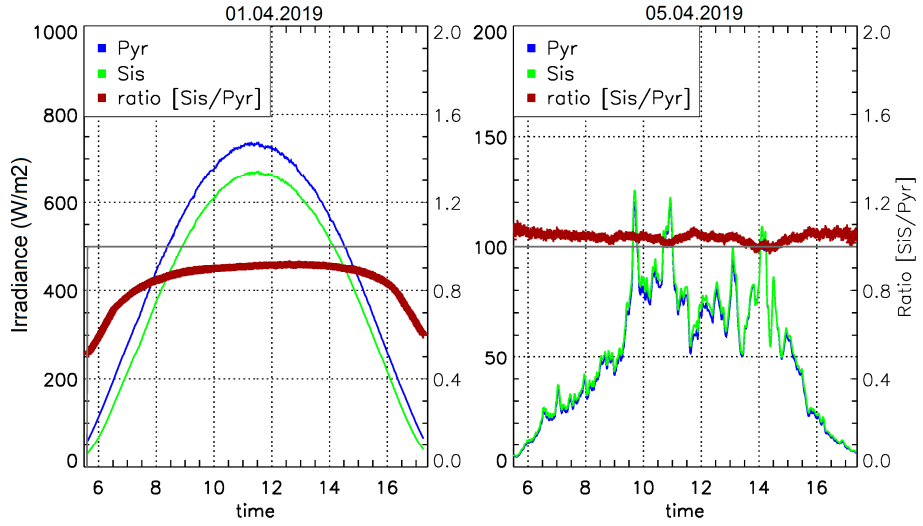

Figure 5. GHI measured by SiS on an overcast day (5 April 2019, **right**) and on a clear sky day (1 April 2019, **left**) and the ratios (SiS/Pyr). Under clear sky conditions, Pyr measured higher than SiS; the difference between sensor increased in the morning and evening hours. The sensitivity of the SiS increased under cloudy conditions due to the change in the spectral distribution of incident diffuse radiation.

Once the sun is totally covered by clouds and the present irradiance is only diffuse, the sensitivity of the SiS increases compared to calibration conditions. The SiS measures a higher solar irradiance than Pyr, which has nearly constant spectral sensitivity over the complete solar spectrum. This result confirms that the spectral distribution of incident solar irradiance significantly impacts the irradiance measured by silicon-based sensors.

It is also worth investigating the influence of these differences between the sensors on the monthly and annual irradiation. Figure 6 shows the average total monthly and annual uncorrected global horizontal irradiation (2016–2019) measured by both sensors.

GHI measured by the thermopile pyranometer was overall higher than the SiS irradiance. The monthly differences ranged between 3.7% in July and 17.1% in January. The annual Pyr irradiation was 6.5% higher.

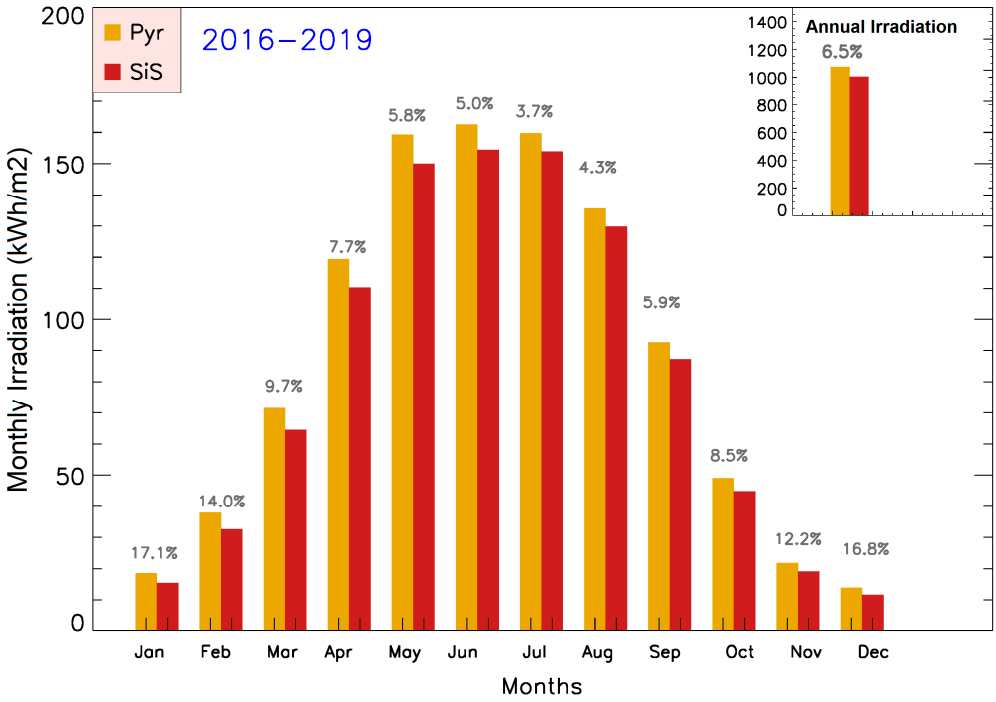

Figure 6. Monthly and annual global irradiation measured by both SiS and Pyr (2016–2019) and the percentage difference between them. The graphics show remarkable variation in monthly irradiation.

The results demonstrate that both sensors measure close to each other. The difference between their readings is minimal during summer months (when solar irradiance level around midday is close to STC value). Once the solar elevation angle decreased in winter months and accordingly, the solar irradiance was lower compared to the STC value, the SiS measured lower than Pyr, and the difference between the sensors was higher. This result agrees with the results achieved in [17].

3. Methods

3.1. Measurement Site

The measurements, which this work is based on, were performed over the course of four years (January 2016–December 2019) on the roof of the Institute for Meteorology and Climatology (IMuK) of the Leibniz Universität Hannover (Hannover, Germany; 52.23° N, 09.42° E and 50 m above sea level). To better evaluate the results, it is necessary to give an overview of the prevailing solar radiation conditions in the measurement site. According to the German Weather Service (DWD), the average annual global horizontal irradiation in Germany (1981–2010) ranges between 951 kWh/m^2 and 1257 kWh/m^2 [35]. Solar radiation in Hannover as a north German city is close to the minimum value, representing a low radiation climate in this region. Ground measurements for GHI at IMUK in the last ten years (2010–2019) showed that the global irradiation ranged between 989 kWh/m^2 and 1162 kWh/m^2 (Figure 7, upper graphic). The results were within the range of DWD.

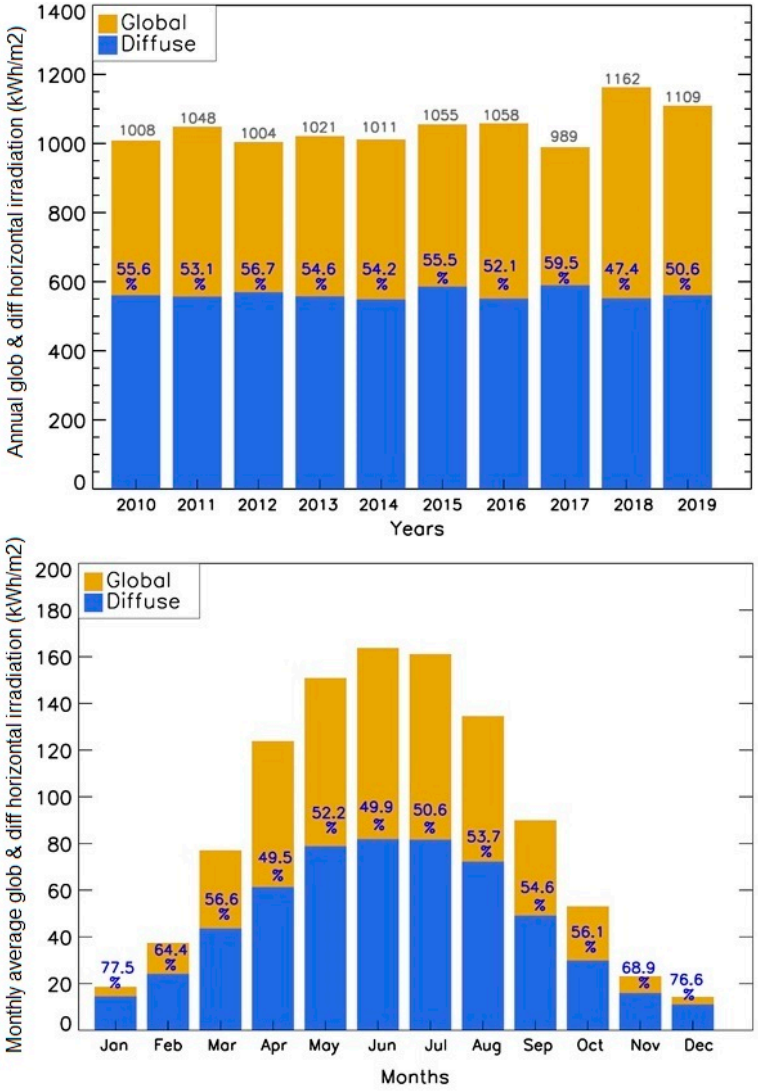

Figure 7. Annual global and diffuse horizontal irradiation in Hannover, measured from 2010 to 2019 (**upper** graphic), and monthly average values, measured in the same period (**lower** graphic). The measurements were performed on the roof of the IMuK by thermopile pyranometers.

The lower graphic of Figure 7 shows the monthly average of global- and diffuse horizontal irradiation in Hannover within the last ten years. GHI had its maximum in June due to the height of the sun and sunshine duration in this month compared to other months. It can be seen that the lowest irradiation values were registered in the winter months when the sunshine duration at its minimum. The monthly average in the summer months was eight to nine times higher than in the winter months. The sun's height is not the main factor that determines the amount of diffuse irradiance, but the atmospheric conditions in the measurement location play an essential role. The monthly diffuse irradiation makes up about half of the global irradiation during summer months and more than two-thirds of global irradiation in winter months. These values can give an idea about the solar radiation climate of Hannover. The big difference between summer and winter irradiation and the distribution of diffuse radiation over the year influences the tilt angle and orientation at which the maximum annual solar radiation is collected.

3.2. Correction Model

One of the aims of this work is to improve the SiS solar irradiance measurements and reduce the difference to the thermopile sensor. Therefore, we proposed a set of correlations

and equations as a correction model to improve the measured SiS-irradiance and to approach the reading of Pyr. The model addressed the main measurement uncertainties that the SiS suffers from in relation to the thermopile pyranometer. The temperature correction was first applied to correct the temperature error caused by changing temperatures during the measurements and the deviation from the STC value. The model started with this correction because the temperature correction depends only on sensor temperature, regardless of sky conditions (clear or cloudy). In the second step, the clear sky data was separated from cloudy-sky conditions using the clearness index (K_t) and SZA. Then cosine, spectral, and calibration corrections were applied according to sky conditions. Figure 8 shows a block diagram of the calculation process of the model.

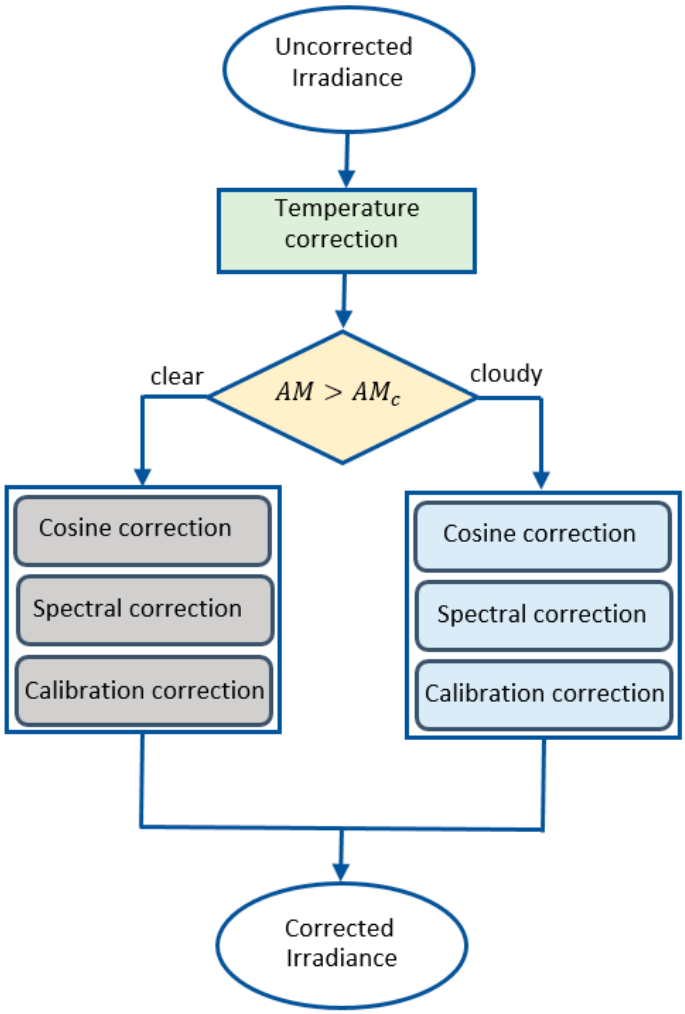

Figure 8. Block diagram of the correction steps in the correction model.

3.2.1. Temperature Correction (C_T)

The daytime temperature of SiS as a reference PV cell differs from the ambient temperature since cells are dark in color and accordingly absorb a greater amount of solar energy [36]. During the day, the silicon sensor becomes hotter than the ambient temperature by a factor that depends on incident solar irradiance. It is known that the short circuit current (I_{sc}) increases with increasing cell temperature [36]. The used silicon sensors operate next to a short circuit [25], and accordingly, the sensor's sensitivity increased as the temperature increase. The influence of temperature on a sensor's response is usually corrected using a temperature coefficient α, which represents the change in I_{sc} with temperature changes related to the temperature value under STC. A typical value of the temperature coefficient for a crystalline silicon (c-Si) PV device is 0.05%/°C [37]. The

temperature coefficient is considered by the manufacturer (IMT), and the correction is done according to Equation (1):

$$(SMM, CosEr, Cf) = \frac{E(T_d,\ SMM, CosEr, Cf)}{1 + \alpha(T_{sen} - 25°C)} \quad (1)$$

where E(T_d,SMM,CosEr,Cf) and E(SMM,CosEr,Cf) are the SiS Irradiance before and after applying the C_T, T_{sen} is the sensor temperature measured by the integrated Pt100 temperature sensor that was mounted to the back of the sensor, and α represents the temperature coefficient (0.05%/°C). The C_T depends only on the sensor's temperature, and therefore, the same correction can be applied to the SiS measurements under all weather conditions.

In the next step, the model separated the clear sky from cloudy measurements. In this work, a combination of the clearness index (K_t) and the SZA was used to separate the clear sky measurements from those measured under cloudy conditions. Figure 9 shows the change in (K_t) with SZA for clear sky and cloudy global irradiances.

$$K_t = \frac{E}{E_0} \quad (2)$$

where E_0 is the extraterrestrial irradiance, and E is the measured global irradiance.

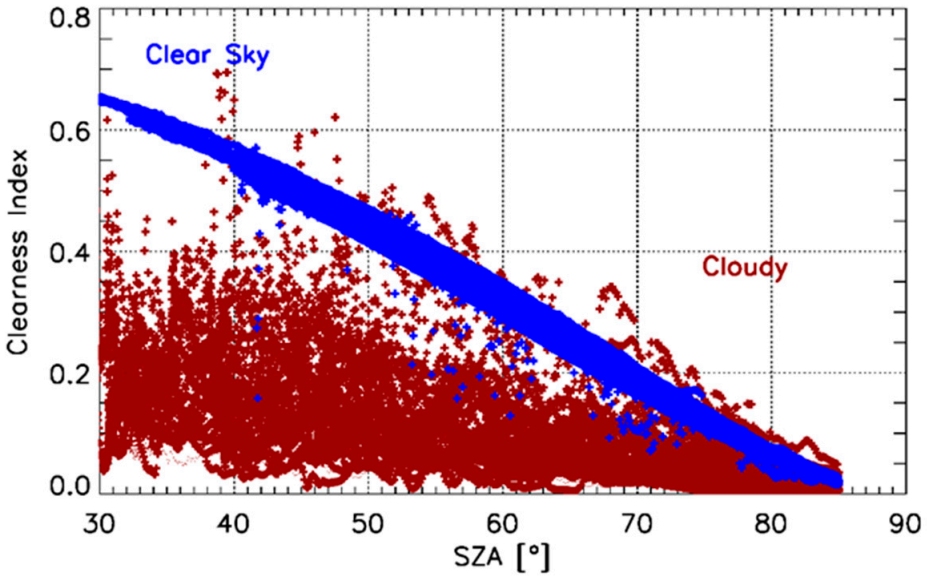

Figure 9. Change in clearness index (K_t) with SZA for clear sky measurements (**blue**) and measurements under cloudy conditions (**brown**) for the year 2019. The clear sky global irradiance has different values of K_t than cloudy measurements under the same SZA.

The extraterrestrial irradiance was calculated as described by Duffie and Beckman (1980) [1]. The values of K_t were different in both cases for the same SZA. We used these differences in the clearness index for each SZA range to separate the clear sky irradiance from those measured under cloudy conditions. Therefore, we defined a critical clearness index value (K_{tc}) for every SZA-range according to Table 2.

Table 2. Separation clear sky global irradiance ($K_t > K_{tc}$) from which measured under cloudy conditions.

SZA Range	Clearness Index
40° > SZA	$K_t > 0.50$
40° < SZA < 50°	$K_t > 0.40$
50° < SZA < 55°	$K_t > 0.30$
55° < SZA < 60°	$K_t > 0.27$
60° < SZA < 65°	$K_t > 0.20$
65° < SZA < 70°	$K_t > 0.15$
70° < SZA < 75°	$K_t > 0.10$
75° < SZA < 80°	$K_t > 0.05$
80° < SZA < 82°	$K_t > 0.04$
82° < SZA < 84°	$K_t > 0.02$
84° < SZA < 85°	$K_t > 0.015$

3.2.2. Cosine Correction (C_c)

Cosine error affects mainly the beam irradiance, while diffuse irradiance has less dependence on SZA. Accordingly, the correction model treated the measurement data differently according to sky conditions. The SiS angular response that was measured in the laboratory of manufacture (Figure 3) was used to correct the clear sky global irradiance. In the case of cloudy days, GHI was corrected for the CosEr using a correction factor, which was obtained as a fit function through empirical measurements. The ratio (E_{SiS}/E_{Pyr}) vs. the SZA is plotted (Figure 10), and a polynomial fitting to the cloudy irradiance tendency was obtained and used to correct the GHI measured in cloudy days according to Equation (3).

$$\mathrm{E(SMM, Cf)} = \frac{\mathrm{E(CosEr, SMM, Cf)}}{-0.0000007(\mathrm{SZA})^3 + 0.00006(\mathrm{SZA})^2 - 0.0009(\mathrm{SZA}) + 0.9856)} \quad (3)$$

where E(CosEr,SMM,Cf) and E(SMM,Cf) are the solar global irradiance before and after applying cosine correction.

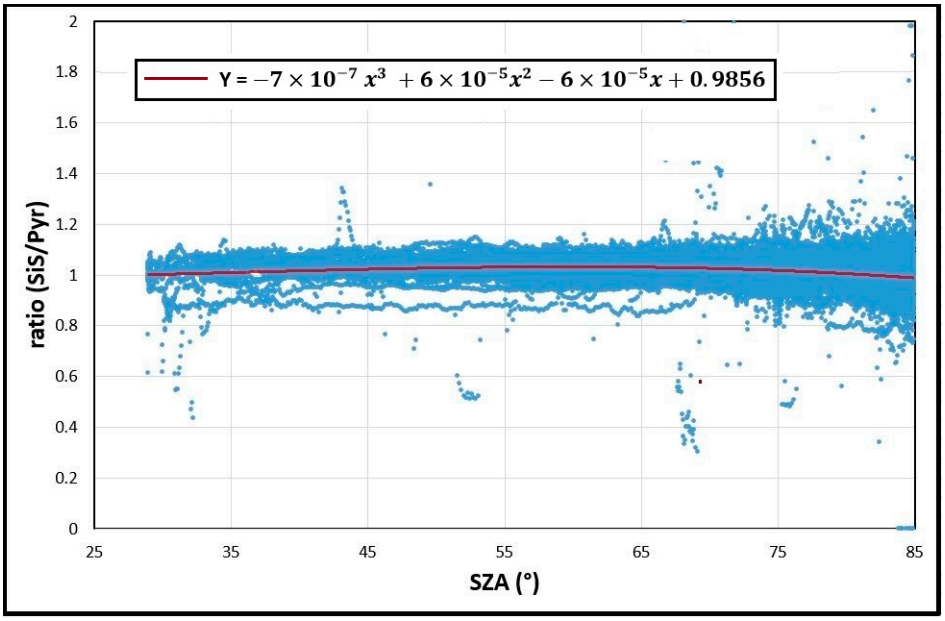

Figure 10. The ration (E_{SiS}/E_{pyr}) under cloudy conditions plotted against SZA. The red line represents the polynomial fit equation of cloudy data.

3.2.3. Spectral Mismatch Correction (C_s)

The spectral distribution of the incident solar irradiance varies during the day, and it is also affected by the atmospheric conditions. As a result, it is generally different from the STC spectrum (AM1.5). These spectral mismatches lead to a measurement uncertainty sometimes noted as spectral mismatch error that is quantified by the spectral mismatch factor (SMM) [38]. The SMM depends on the semiconductor materials used in PV sensors and the atmospheric conditions in terms of cloud cover and aerosol content [13,39]. The spectral distribution of the beam irradiance differs from that of the diffuse irradiance. Accordingly, spectral mismatch affects both irradiance components differently. The model treated the spectral mismatch of clear sky measurements in a way that differed from cloudy conditions.

One way to determine the magnitude of SMM of the sensor under clear sky conditions is to measure the spectral distribution over the day and compare it to the AM1.5 spectral distribution that is used for the calibration. The air mass is calculated using the formula of Kasten and Young [40]. Due to the unavailability of simultaneous spectral measurements, we calculated the spectral irradiance in this work using the UVSPEC model in the Libradtran package [41,42]. As an input parameter, horizontal visibility of 20 km, perceptible water of 15 kg/m^2, an albedo of 0.02, and a total ozone column of 300 DU were used (Figure 11, left). First, the pyranometer irradiance (E_{Pyr}) was calculated, and then the SiS irradiance (E_{SiS}) was determined according to Equations (4) and (5). Then the spectral irradiances at AM1.5 were calculated and used as reference values for both sensors ($E_{Pyr.cal}$, $E_{SiS.cal}$). The spectral mismatch factor was calculated according to Equation (8),

$$E_{Pyr} = \int_{285}^{2800} E(\lambda) d\lambda \tag{4}$$

$$E_{SiS} = \int_{360}^{1200} E(\lambda) SR(\lambda) d\lambda \tag{5}$$

$$E_{Pyr.cal} = \int_{285}^{2800} E_{AM1.5}(\lambda) d\lambda \tag{6}$$

$$E_{SiS.cal} = \int_{360}^{1200} E_{AM1.5}(\lambda) SR(\lambda) d\lambda \tag{7}$$

$$\text{SMM} = \frac{\int_{360}^{1200} E(\lambda) SR(\lambda) d\lambda \,.\, \int_{285}^{2800} E_{AM1.5}(\lambda) d\lambda}{\int_{285}^{2800} E(\lambda) d\lambda \,.\, \int_{360}^{1200} E_{AM1.5}(\lambda) SR(\lambda) d\lambda} \tag{8}$$

where, $E_{AM1.5}$ is the spectral irradiances at AM1.5.

The corrected irradiance was then calculated by dividing the uncorrected value by the SMM:

$$E(Cf) = \frac{E(SMM, Cf)}{SMM} \tag{9}$$

where *E(SMM,Cf)*, *E(Cf)* are the solar irradiance before and after applying the spectral correction.

For cloudy days, the SMM was obtained as a fit function through empirical measurements. The ratio (E_{SiS}/E_{Pyr}) vs. the air mass is plotted in Figure 11 (right), and a polynomial fitting to the cloudy irradiance tendency was obtained and used to correct the GHI measured in cloudy days according to Equation (10).

$$E(Cf) = \frac{E(SMM, Cf)}{\left(0.0029(AM)^2 - 0.0001\ (AM) + 1.0144\right)} \tag{10}$$

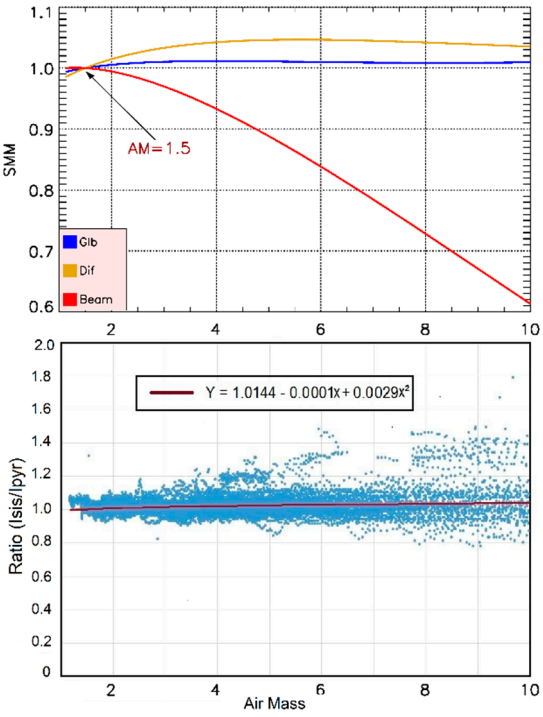

Figure 11. The spectral mismatch factor SMM for global, diffuse, and beam irradiances plotted against AM (upper graphic). The calculations were based on the radiative transfer model libRadtran under clear sky conditions. Lower graphic shows the ratio (E_{SiS}/E_{Pyr}) under cloudy conditions plotted against AM. The red line represents the polynomial fit equation for cloudy data.

It is essential to refer here that the SMM may be strongly influenced by the atmospheric conditions and the PV semiconductor materials [39].

3.2.4. Calibration Correction (C_{cal})

The calibration of silicon sensors was carried out under STC: 1000 W/m^2 of irradiance, AM1.5 spectrum, and 25 °C of cell temperature. In fact, these reference conditions were hardly obtainable in the outdoor measurements as they combined the irradiance of a clear summer day with the sensor temperature of a clear winter day and the spectrum of a clear spring day. Operating the sensors under real atmospheric conditions that deviate from the STC introduces a calibration error. This deviation depends on the real atmospheric conditions that were changing continuously, making the exact evaluation of the error more complicated. We calculated the calibration deviation factor for both clear and cloudy conditions differently in this work. The most influential parameter that affected the calibration factor's magnitude was the solar irradiance prevailing in the field. Calibration factor correction for clear sky conditions (*Cf-cl*) was calculated by comparing the irradiance measured by both sensors around noontime (about ± 60 min). The calculations were performed after applying the temperature, cosine, and spectral mismatch corrections.

The calibration correction factor (C_{cal}) was calculated by plotting the ratio (E_{SiS}/E_{Pyr}) vs. the SZA_{min} (as the irradiance is maximum) and obtaining the correlation equation as a linear fit. The obtained equation was then multiplied by SiS irradiance according to Equation (11):

$$E_{corr} = E(Cf - cl) * (0.0009(SZA_{min}) + 1.0005) \quad (11)$$

where *E(Cf-cl)*, E_{corr} are the solar irradiance before and after applying the calibration correction for clear sky measurements and SZA_{min} is the minimum daily SZA value.

In the case of cloudy conditions, there was, unfortunately, no reliable cloudy diffuse reference to which the measurements could be compared. Thus, the calibration factor was obtained as a fit function through empirical measurements. The ratio (E_{SiS}/E_{Pyr}) vs.

the SZA was plotted (after applying the other corrections), and a correlation equation was applied as a correction factor to correct the GHI measured under cloudy conditions Equation (12).

$$E_{corr} = \frac{E(Cf - cd)}{(0.0006(SZA) + 0.969)} \quad (12)$$

where *E(Cf-cd)*, (E_{corr}) are the overcast irradiance before and after applying calibration correction.

4. Results and Discussion

This section presents the results of applying the correction model on SiS measurements. We will start by investigating the effect of individual corrections, namely temperature, cosine, spectral, and calibration corrections, as well as evaluating the magnitude of each correction on the measured irradiance. Finally, we apply all corrections on the SiS measurements and compare them to the Pyr irradiance before and after applying the corrections.

Figure 12 describes the influence of individual correction factors on the measured SiS irradiance for two clear sky days. The two case-study days on 29 June (upper graphic) and 16 April (lower graphic) were chosen to investigate the influence of the model on clear sky conditions in different temperatures and solar heights. The value of temperature correction affected the measured irradiance according to sensor temperature with relation to calibration value (green curve). When sensor temperature exceeded the calibration value (25 °C), the SiS measured higher values than it should be, and then the purpose of C_T was to reduce the SiS irradiance.

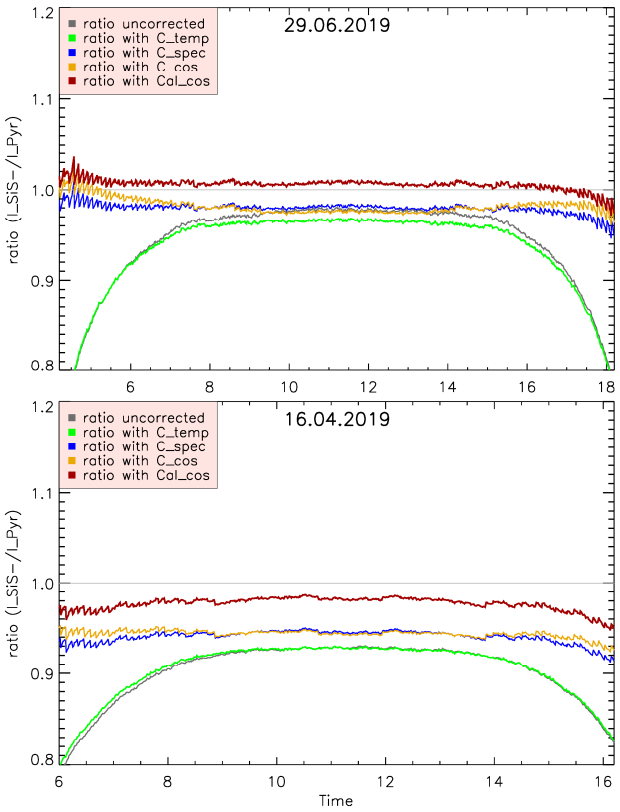

Figure 12. The daily curve of the ratio (E_{SiS}/E_{Pyr}) for two clear sky days (16 April 2019, 29 June 2019) before (gray) and after applying each step of the correction model. The corrections were applied to the raw data one after another. First, the temperature correction was applied (green), then cosine correction (gold), then spectral correction (blue), and finally, the calibration correction (brown).

The reduction had its maximum at about noon when the irradiance and thus the temperatures were at maximum. The influence of C_T decreased with increasing SZA, where the temperatures decreased. Once the temperature was below 25 °C, C_T had an increasing influence on SiS irradiance (Figure 10, right).

Due to a large cosine error of the used silicon sensors, the cosine correction played the greatest role in correcting the SiS irradiance (golden curve). The losses of SiS irradiance due to cosine error were the highest under clear sky conditions, as shown in Figure 12. C_c increased the SiS irradiance depending on the SZA, and its influence was strongest in early mornings and late afternoons.

The blue curve shows the influence of spectral mismatch correction on the SiS irradiance after applying the temperature and cosine corrections. C_s increased the SiS irradiance as long as the AM was below the calibration value (AM1.5). Once the air mass exceeded 1.5, the path of solar radiation through the atmosphere was longer, and the incident radiation contained more red light. Accordingly, the response of SiS irradiance increased compared to STC, and then the purpose of C_s was to decrease the SiS irradiance. Therefore, the blue curve on both days under study lay above the golden curve around noontime (Am < 1.5) and lay below in the morning and evening hours (Am > 1.5). In general, the spectral mismatch showed seasonal variation depending on the semiconductor material of the sensor [2]. The spectral effect of the SiS (C-si) was smaller, and there was a small seasonal variation [2,3]. Applying the correction model on the SiS measurements under clear sky conditions increased the SiS irradiance (independent of the time of the day) and thus decreased the difference to the Pyr irradiance.

The influence of the correction model on the monthly and annual values is shown in Figure 13. The deviation of the SiS irradiation from the Pyr values decreased significantly after applying the correction model on the SiS measurements. The differences in total annual irradiation decreased from 70 KWh/m^2 to 15 kWh/m^2 with the correction.

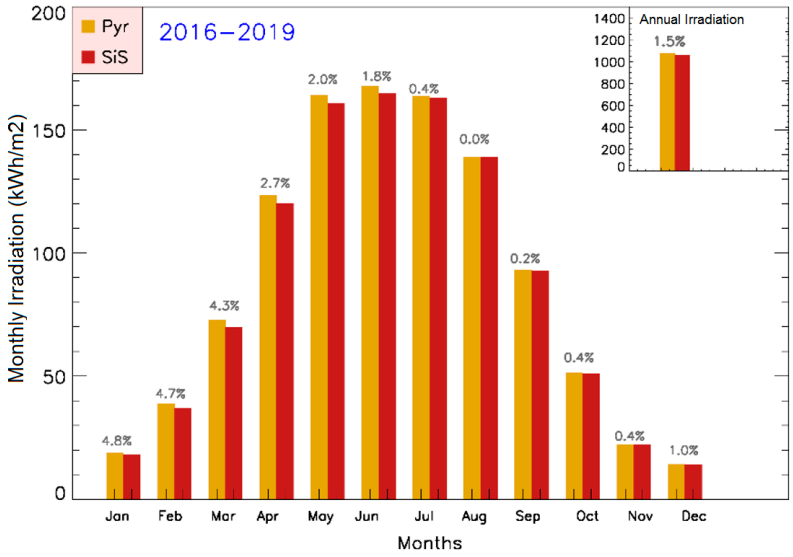

Figure 13. Monthly and annual differences between SiS and Pyr GHI (2016–2019) after applying the correction model on SiS measurements. The differences between the sensor readings decreased significantly after the correction. The difference in total annual irradiation between the sensor readings decreased from 6.5% to 1.5%.

The ability of the model to decrease the difference between the sensors under cloudy conditions was limited due to the anisotropic distribution of sky radiation and a combination of multiple influencing factors. Figure 14 shows the results of applying the correction model on an overcast day, 16 September 2019. It can be seen that the temperature and cosine corrections had a small increasing influence on the SiS irradiance due to the low

sensor temperature (below 25 °C) and the cosine error of the sensor. On the other hand, the spectral correction decreased the irradiance due to the high AM values. However, applying the model to the measurements decreased the SiS irradiance and reduced the difference to the Pyr irradiance.

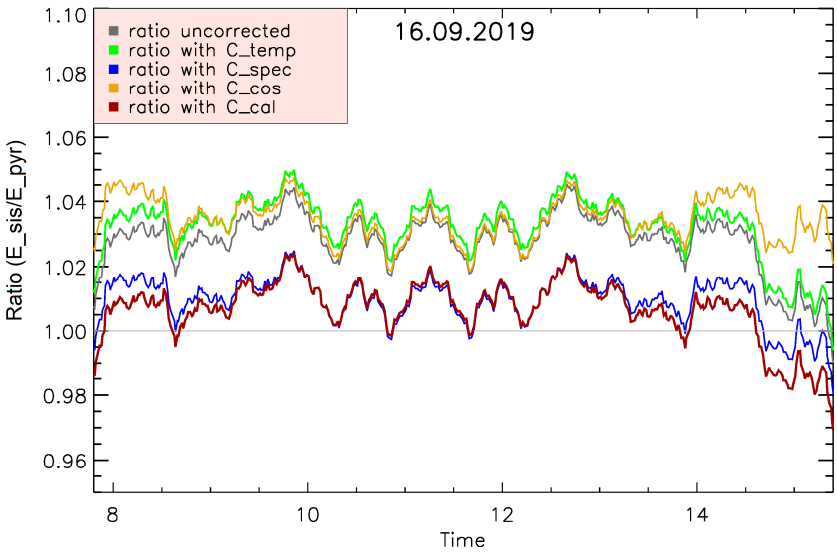

Figure 14. The daily curve of the ratio (E_{SiS}/E_{Pyr}) for an overcast day (16 September 2019) before (**gray**) and after applying each step the correction model. First, the temperature correction was applied (**green**), then cosine (**gold**) and spectral correction (**blue**), and finally the calibration correction (**brown**).

The ability of the correction model to correct the GHI measured by the SiS was also analyzed by means of the relative Root Mean Square Difference (rRMSD) and relative Mean Absolute Difference (rMAD). Table 3 shows the average deviation of the sensors' readings after each correction step. The rRMSD of daily irradiation between SiS and Pyr decreased from 10.6% to 5.4% after applying the correction model, while the rMAD values decreased from 7.4% to 2.5%.

Table 3. Statistical indices of the daily irradiation after each correction step, compared to Pyr measurements.

	Ucalb	C_T	C_c	C_s	C_{Tcal}
rRMSD (%)	10.6	10.8	7.5	7.6	5.4
rMAD (%)	7.4	7.6	4.7	4.8	2.5

5. Conclusions

In this work, we focused on the differences between two of the commonly used solar sensors: thermopile pyranometer and silicon-based sensor. These sensors were different in the used technology, measuring principle, and responses to incident solar irradiance. Therefore, the values of irradiance measured with these sensors were different. We aimed to analyze these differences in order to propose a method to improve the SiS measurements by minimizing the difference between SiS and Pyr readings using the minimum number of input parameters. Reducing the errors of silicon-based sensors can open a new avenue for using these sensors as low-cost irradiance sensors. We discussed four parameters that influence the sensor measurements, namely the temperature, cosine error, spectral mismatch, and calibration factor. In order to eliminate the uncertainty caused by these parameters, a correction model based on the analysis was applied to SiS measurements.

Applying the temperature correction on the SiS measurements increased the measured value of irradiance in the winter months when the cell temperature was below the calibration value (25 °C). On the other hand, the correction caused a decrease in the measured value of SiS irradiance on hot days when cell temperatures were above 25 °C.

In comparison to temperature and spectral corrections, the effect of cosine error correction on the SiS irradiance was greater due to a large cosine error of the silicon sensors under investigation for SZAs larger than 60°, which is shown in Figure 12. The influence of this correction appeared to be more marked at sunsets and sunrises of clear sky days. Cosine error affects mainly the beam irradiance, while diffuse irradiance had less dependence on SZA.

Spectral mismatch correction increases or decreases the SiS irradiance, depending on the air mass with respect to the AM1.5 spectrum used in STC. For AM values below AM1.5, the correction increased the SiS irradiance. For air mass higher than AM1·5, the spectral distribution of the global solar irradiance changed in favor of the spectral response of SiS. Accordingly, the correction decreased the measured SiS irradiance (Figure 12, blue curve). The spectral mismatch and the spectral correction were strongly influenced by the used PV material and atmospheric conditions.

The model applied as a last correction the calibration factor correction that stems from calibration of SiS under STC, which deviated from the real atmospheric conditions. The magnitude of this correction in clear sky days depends on the solar irradiance; its value is greater in winter months than in summer months. This correction increased the SiS irradiance in clear sky conditions by 2–5% and decreased by up to 3% for overcast conditions.

As a result of applying the correction model on the GHI of SiS, the differences between the values measured with both sensors were reduced significantly. The daily rRMSD between SiS and Pyr irradiances decreased from 10.6% to 5.4% after applying the correction model, while the rMAD decreased from 7.4% to 2.5%.

The differences in the total annual GHI decreases from 70 KWh/m^2 (6.5%) to 15 kWh/m^2 (1.5%) by the correction.

The model was used to correct the GHI measurements. The accuracy of the model for correcting tilted irradiance was not tested due to the unavailability of thermopile measurements on inclined surfaces. However, we assumed that this model can be used to correct the SiS irradiance measured on tilted surfaces. The assumption is based on the fact that the temperature factor depends only on the sensor temperature and the cosine error depends on the angle of incident (AOI). In addition, the spectral mismatch factor has a negligible dependence on the tilt angle of the sensor [2], and the calibration factor depends on the level of incident irradiance.

It can be concluded that applying the correction model on the SiS irradiance significantly reduces the differences between the readings of the sensors and makes the SiS more useful as a low-cost instrument to measure GHI.

Author Contributions: R.M. conceived and designed the study and wrote the draft paper; H.S. contributed to the discussion, collected the data, and supervised the measurements; G.S. contributed to the conception and discussion of the data. All authors significantly contributed to the final version of the manuscript. All authors have read and agreed to the published version of the manuscript.

Funding: The APC was funded by the Open Access fund of Leibniz Universität Hannover.

Acknowledgments: The publication of this article was funded by the Open Access fund of Leibniz Universität Hannover. We are grateful to Christian Melsheimer from IUP Bremen for improving the English.

Conflicts of Interest: The authors declare no conflict of interest.

Nomenclature

GHI	Global Horizontal Irradiance
DHI	Diffuse Horizontal Irradiance
AM	Air Mass
Pyr	Thermopile Pyranometer
SiS	Silicon Sensor
SR	Spectral Response
Δ	difference between cell temperature and STC value (25 °C)
α	temperature coefficient
K_t	Clearness Index
SZA	Solar Zenith Angle
λ	Wavelength of Irradiance
Tf	Temperature factor
MFF	Spectral Mismatch Factor
CosEr	Cosine error
Cf	Calibration factor
T_{sen}	Temperature of Sensor
E	Global Irradiance
SZA_{min}	Minimum Solar Zenith Angle
C_T	Temperature correction
C_s	Spectral correction
C_c	Cosine correction
C_{cal}	Calibration correction
I_{sc}	Short circuit current

References

1. Wright, S. Second Law Analysis of the Earth System with a Radiative Model. *Int. J. Thermodyn.* **2002**, *5*, 57–65.
2. El-Shirbeny, M.A.; Abdellatif, B. Reference evapotranspiration borders maps of Egypt based on kriging spatial statistics method. *Int. J. Geomate* **2017**, *13*, 37. [CrossRef]
3. Spertino, F.; di Leo, P.; Cocina, V. Accurate measurements of solar irradiance for evaluation of photovoltaic power profiles. In Proceedings of the 2013 IEEE Grenoble Conference PowerTech, Powertech 2013, Grenoble, France, 16–20 June 2013.
4. Pereira, G.M.S.; Stonoga, R.L.B.; Detzel, D.H.M.; Küster, K.K.; Neto, R.A.P.; Paschoalotto, L.A.C. Analysis and Evaluation of Gap Filling Procedures for Solar Radiation Data. In Proceedings of the 2018 IEEE 9th Power, Instrumentation and Measurement Meeting, EPIM 2018, Salto, Uruguay, 14–16 November 2018.
5. IPCC. Climate Change 2007-The Physical Science Basis: Working Group I Contribution to the Fourth Assessment Report of the IPCC. *Science* **2007**, *4*, 8117.
6. Kopp, G.; Lean, J.L. A new, lower value of total solar irradiance: Evidence and climate significance. *Geophys. Res. Lett.* **2011**, *1*, 38. [CrossRef]
7. Paulescu, M.; Paulescu, E.; Gravila, P.; Badescu, V. Weather Modeling and Forecasting of PV Systems Operation. *Green Energy Technol.* **2013**, *5*, 232.
8. Wilbert, S.; Geuder, N.; Schwandt, M.; Kraas, B.; Jessen, W.; Meyer, R.; Nouri, B. *Best Practices for Solar Irradiance Measurements with Rotating Shadowband Irradiometers*; International Energy Agency: Paris, France, 2015.
9. Dunn, L.; Gostein, M.; Emery, K. Comparison of pyranometers vs. PV reference cells for evaluation of PV array performance. In Proceedings of the Conference Record of the IEEE Photovoltaic Specialists Conference, Austin, TX, USA, 3–8 June 2012.
10. Meydbray, J.; Riley, E.; Dunn, L.; Emery, K.; Kurtz, S. *Pyranometers and Reference Cells: Part 2: What Makes the Most Sense for PV Power Plants*; National Renewable Energy Lab: Golden, CO, USA, 2012.
11. Azouzoute, A.; Merrouni, A.A.; Bennouna, E.G.; Gennioui, A. Accuracy measurement of pyranometer vs reference cell for PV resource assessment. *Energy Procedia* **2019**, *157*, 1201–1209. [CrossRef]
12. Alados-Arboledas, L.; Batlles, F.J.; Olmo, F.J. Solar radiation resource assessment by means of silicon cells. *Sol. Energy* **1995**, *54*, 183–191. [CrossRef]
13. King, D.L.; Myers, D.R. Silicon-photodiode pyranometers: Operational characteristics, historical experiences, and new calibration procedures. In Proceedings of the Conference Record of the IEEE Photovoltaic Specialists Conference, Anaheim, CA, USA, 3 October 1997.
14. Vignola, F. Removing systematic errors from rotating shadowband pyranometer data. In Proceedings of the American Solar Energy Society-Solar 2006: 35th ASES Annual Conf., 31st ASES National Passive Solar Conference, 1st ASES Policy and Marketing Conf., ASME Solar Energy Division Internationnal Solar Energy Conference, Denver, CO, USA, 13 July 2006.
15. Geuder, N.; Pulvermüller, B.; Vorbrugg, O. Corrections for rotating shadowband pyranometers for solar resource assessment. In Proceedings of the Optical Modeling and Measurements for Solar Energy Systems II, San Diego, CA, USA, 11 September 2008.

16. Forstinger, A. Physically based correction of systematic errors of Rotating Shadowband Irradiometers. *Meteorol. Z.* **2020**. Available online: https://elib.dlr.de/121698/1/__ASFS01_Group_Literature_Database_SolarResearch.Data_PDF_Bachelorthesis_Forstinger-1058268416_Bachelorthesis_Forstinger.pdf (accessed on 21 March 2021). [CrossRef]
17. Mubarak, R.; Hofmann, M.; Riechelmann, S.; Seckmeyer, G. Comparison of modelled and measured tilted solar irradiance for photovoltaic applications. *Energies* **2017**, *10*, 1688. [CrossRef]
18. Mubarak, R.; Luiz, E.W.; Seckmeyer, G. Why PV modules should preferably no longer be oriented to the south in the near future. *Energies* **2019**, *12*, 4528. [CrossRef]
19. International Organization for Standardization. *ISO 9060: Solar Energy-Specification and Classification of Instruments for Measuring Hemispherical Solar and Direct Solar Radiation*; International Organization for Standardization: Geneva, Switzerland, 1990.
20. CMP11 Secondary Standard Pyranometer-Kipp & Zonen. Available online: https://www.kippzonen.com/Product/13/CMP11-Pyranometer#.YFdMeucxlaQ (accessed on 21 March 2021).
21. Vignola, F.; Peterson, J.; Chiu, C.Y.; Dooraghi, M.; Sengupta, M.; Mavromatakis, F. Comparison of pyranometers and reference cells on fixed and one-Axis tracking surfaces. In Proceedings of the ASES SOLAR 2017-46th Annual National Solar Conference, Denver, CO, USA, 9–12 October 2017.
22. Vignola, F.; Peterson, J.; Kessler, R.; Dooraghi, M.; Sengupta, M.; Mavromatakis, F. Evaluation of Photodiode-based Pyranometers and Reference Solar Cells on a Two-Axis Tracking System. In Proceedings of the 2018 IEEE 7th World Conference on Photovoltaic Energy Conversion, WCPEC 2018-A Joint Conference of 45th IEEE PVSC, 28th PVSEC and 34th EU PVSEC, Waikoloa, HI, USA, 10–15 June 2018.
23. King, D.L.; Boyson, W.E.; Hansen, B.R. *Improved Accuracy for Low-Cost Solar Irradiance Sensors*; Sandia National Labs.: Albuquerque, NM, USA, 1997.
24. Myers, D.R.; Emery, K.A.; Stoffel, T.L. Uncertainty estimates for global solar irradiance measurements used to evaluate PV device performance. *Sol. Cells* **1989**, *27*, 455–464. [CrossRef]
25. Si Sensor: Ingenieurbüro Mencke & Tegtmeyer GmbH. Available online: https://www.imt-solar.com/solar-irradiance-sensors/si-sensor/ (accessed on 21 March 2021).
26. Dutton, E.G.; Michalsky, J.J.; Stoffel, T.; Forgan, B.W.; Hickey, J.; Nelson, D.W.; Alberta, T.L.; Reda, I. Measurement of the broadband diffuse solar irradiance using current commercial instrumentation with a correction for thermal offset errors. *J. Atmos. Ocean. Technol.* **2001**, *18*, 297–314. [CrossRef]
27. Reda, I.; Stoffel, T.; Myers, D. A method to calibrate a solar pyranometer for measuring reference diffuse irradiance. *Sol. Energy* **2003**, *74*, 103–112. [CrossRef]
28. Michalsky, J.J.; Harrison, L.; LeBaron, B.A. Empirical radiometric correction of a silicon photodiode rotating shadowband pyranometer. *Sol. Energy* **1987**, *39*, 87–96. [CrossRef]
29. Perraki, V.; Kounavis, P. Effect of temperature and radiation on the parameters of photovoltaic modules. *J. Renew. Sustain. Energy* **2016**, *8*, 013102. [CrossRef]
30. Iqbal, M. *An Introduction to Solar Radiation*; Elsevier: Amsterdam, The Netherlands, 2012.
31. Michalsky, J.J.; Harrison, L.C.; Berkheiser, W.E. Cosine response characteristics of some radiometric and photometric sensors. *Sol. Energy* **1995**, *54*, 397–402. [CrossRef]
32. Zibordi, G.; Bulgarelli, B. Effects of cosine error in irradiance measurements from field ocean color radiometers. *Appl. Opt.* **2007**, *46*, 5529–5538. [CrossRef] [PubMed]
33. Cordero, R.R.; Seckmeyer, G.; Labbe, F. Cosine error influence on ground-based spectral UV irradiance measurements. *Metrologia* **2008**, *45*, 406. [CrossRef]
34. Kipp, Z. Solar Radiation Measurements for Solar Energy Applications. Available online: file:///C:/Users/MDPI/AppData/Local/Temp/KippZonen_Solar_Energy_Guide-1.pdf (accessed on 21 March 2021).
35. Wetter und Klima-Deutscher Wetterdienst-Our Services-Maps of Global Radiation, Monthly and Annual Sum. Available online: https://www.dwd.de/EN/ourservices/solarenergy/maps_globalradiation_sum.html?nn=495490 (accessed on 1 April 2021).
36. Elminir, H.; Benda, V.; Tousek, J. Effects of solar irradiation conditions and other factors on the outdoor performance of photovoltaic modules. *J. Electr. Eng.* **2001**, *52*, 125–133.
37. Shukla, A.K. *Experimental Methods in the Physical Sciences*; Elsevier: Amsterdam, The Netherlands, 2009.
38. Huang, X.; Quan, C.; Kng, J. Comparison of two methods for short circuit current measurement of large size solar cell. In Proceedings of the International Conference on Optical and Photonic Engineering (icOPEN2015), Singapore, 17 July 2015; p. 95242A.
39. Stark, C.; Theristis, M. The impact of atmospheric parameters on the spectral performance of multiple photovoltaic technologies. In Proceedings of the 2015 IEEE 42nd Photovoltaic Specialist Conference (PVSC), New Orleans, LA, USA, 14–19 June 2015; pp. 1–5.
40. Kasten, F.; Young, A.T. Revised optical air mass tables and approximation formula. *Appl. Opt.* **1989**, *28*, 4735–4738. [CrossRef] [PubMed]
41. Mayer, B.; Kylling, A. Technical Note: The libRadtran Software Package for Radiative Transfer Calculations-Description and Examples of Use. *Atmos. Chem. Phys.* **2005**, *5*, 1855–1877. [CrossRef]
42. Amillo, A.M.G.; Huld, T.; Vourlioti, P.; Müller, R.; Norton, M. Application of satellite-based spectrally-resolved solar radiation data to PV performance studies. *Energies* **2015**, *8*, 3455–3488. [CrossRef]